PROCEEDINGS, 44th Workshop on Geothermal Reservoir Engineering
Stanford University, Stanford, California, February 11-13, 2019
SGP-TR-214

Geothermal Reservoir Imaging Using 2016 Walkaway VSP Data from the Raft River Geothermal Field

Benxin Chi and Lianjie Huang

Los Alamos National Laboratory, Los Alamos, NM 87545, USA

benxinchi@lanl.gov ; ljh@lanl.gov

Keywords: Enhanced geothermal system, elastic-waveform inversion, least-squares reverse-time migration, Narrows zone, Raft River geothermal field, velocity model, vertical seismic profiling, VSP, walkaway

ABSTRACT

The Raft River geothermal field was selected by the U.S. Department of Energy (DOE) as an Enhanced Geothermal System (EGS) demonstration project in 2010. Reliable geothermal reservoir characterization requires high-resolution subsurface imaging. A vertical seismic profile (VSP) survey was conducted along five walkaway lines in 2016. We build a 3D velocity model using 3D elastic-waveform inversion of the five walkaway VSP data. The 3D velocity model reveals a low-velocity zone, which may be associated with the Narrows zone, a fractured zone for EGS stimulation. We then apply 3D least-squares elastic reverse-time migration to the five walkaway VSP data and obtain a high-resolution subsurface image, showing detailed subsurface structures surround the Narrows zone. Our results demonstrate that 3D elastic-waveform inversion and 3D least-squares elastic reverse-time migration of walkaway VSP data can produce useful subsurface information for geothermal reservoir imaging and characterization.

1. INTRODUCTION

The Raft River geothermal field is located in southern Idaho approximately 100 miles northwest of Salt Lake City, Utah (Figure 1). This geothermal field was selected by the U.S. Department of Energy (DOE) as an Enhanced Geothermal System (EGS) demonstration project in 2010. There are four production wells in the Raft River geothermal field: RRG 1, 2 and 4 located on the northwest side of the field (Figure 1) and RRG-7 located on the southeast side. From geophysical data (Mabey et al., 1978), researchers have inferred that the geothermal production of the area originates in the Precambrian basement located between depths of 1400 to 1750 m (Ayling et al., 2011; Jones et al., 2011). Ayling et al. (2011) performed geochemical analysis on the geothermal reservoir fluids and found that the geochemistry of the fluid collected from the southeast region of the field differed from the geochemistry of the fluid collected in northwest regions of the field. The reservoir fluids collected from the northwest (RRG-1,2,4,5) contain lower salinities than those collected from the southeast (RRG-3,6,7,9,11). Based on geochemical data analysis, Ayling and Moore (2013) concluded that the northwestern and southeastern portions of the geothermal field are separated by a low permeability shear zone located within the Precambrian basement. This low permeability shear zone is referred to as the Narrows zone (Figure 2). The presence of the Narrows zone is supported by microearthquake data collected since August, 2010 (Figure 2) by Lawrence Berkeley National Laboratory (LBNL). Accurate imaging and characterization of the Narrows zone is necessary for EGS development at the Raft River geothermal field.

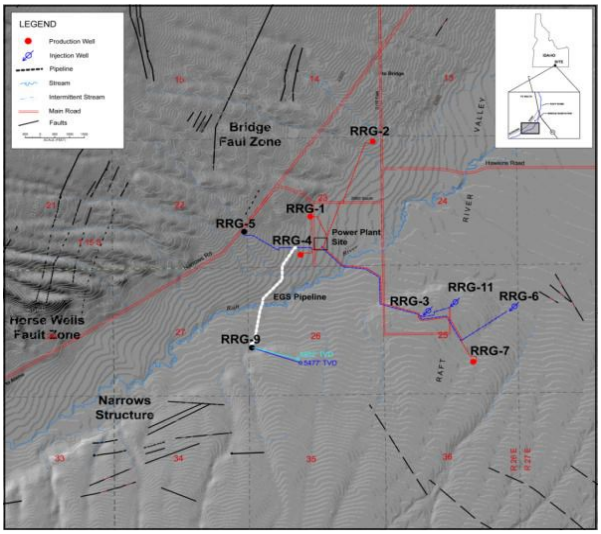

Figure 1: Map of the Raft River geothermal field. Production wells and production pipelines are shown in red. Injection wells and injection pipelines are shown in blue. Well RRG-9 was used for VSP data acquisition (Modified from Williams et al., 1982).

We carried out a three-component vertical seismic profiling (VSP) survey in 2016 along five walkaway lines using borehole geophones in Well RRG-9 at the Raft River geothermal field. The goals of this survey are to build a high-resolution velocity model of the region and image the geothermal reservoir. This high-resolution velocity model can be used for accurate microearthquake imaging and focal mechanism inversion, and for the high-resolution migration imaging of the VSP data. Chi and Huang (2018a and 2018b) carried out the elastic-waveform inversion and least-squares reverse-time migration using the VSP data from sources located approximately along a northwest to southeast trending line (Line 4 and Line 8). To obtain a high-resolution velocity model for the whole Raft River geothermal region, we apply our recently developed multiscale elastic-waveform inversion method to the VSP data along all five walkaway lines to invert for both P- and S-wave velocity models. To image the geothermal reservoir, we apply our recently developed elastic least-squares reverse-time migration (ELSRTM) method to the VSP data to obtain high-resolution P- and S-images.

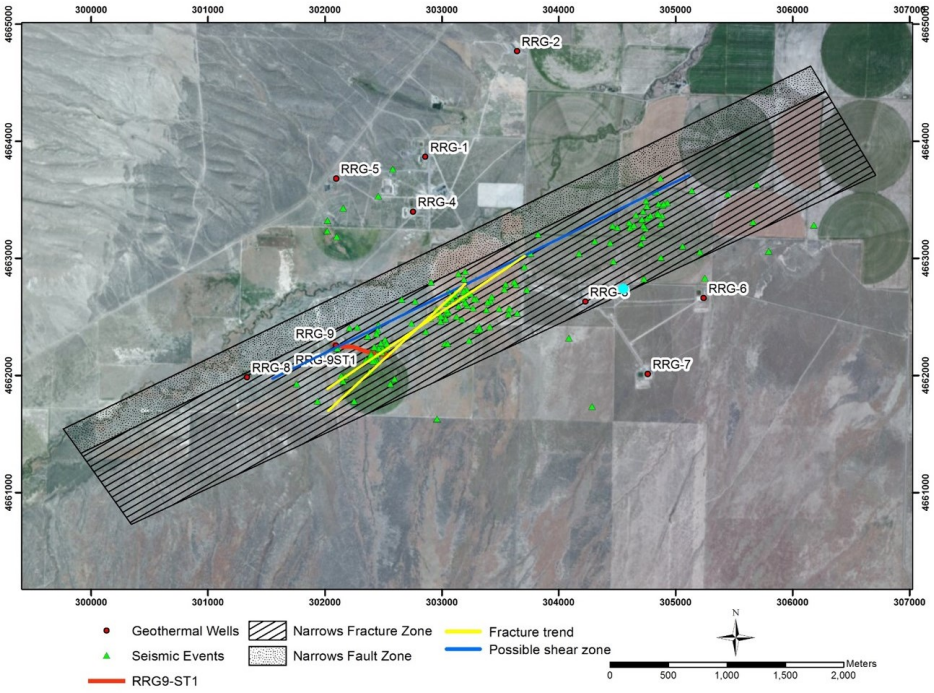

Figure 2: Distribution of microearthquake events since August, 2010 along the Narrows zone at the Raft River geothermal field (Li et al., 2017).

We organize the paper as the following. We first briefly describe the inversion methods used, present example VSP data for inversion, build a 1D velocity model from sonic log data, and give traveltime tomography and multiscale elastic-waveform inversion results obtained using five walkaway lines VSP data acquired at the Raft River geothermal field in 2016. Finally, we show the high resolution P- and S-images obtained using elastic least-squares reverse-time migration. Both our inversion models and migration images confirm the existence of the Narrows zone.

2. METHODS

2.1 3D Adjoint-State First-Arrival Traveltime Tomography

The adjoint-state first-arrival traveltime tomography (FATT) is a nonlinear minimization problem formulated as (1)

$$E(\mathbf{m}) = \arg\min\left(T_{obs} - T(\mathbf{m})\right)^2, \tag{1}$$

where T_{obs} is the observed first-arrival traveltime, and $T(\mathbf{m})$ is the synthetic first-arrival traveltime computed using the eikonal equation in the isotropic model $\mathbf{m} = v(\mathbf{x})$:

$$\left|\nabla T(\mathbf{x})\right|^2 = \frac{1}{v^2(\mathbf{x})}. \tag{2}$$

We employ the fast-sweeping method to solve the eikonal equation. To be complete, the fast sweeping in the 3D case consists of eight alternating sweeping directions:

$$\begin{array}{l} I=1:N_1, J=1:N_2, K=1:N_3 \\ I=1:N_1, J=1:N_2, K=N_3:1 \\ I=1:N_1, J=N_2:1, K=1:N_3 \\ I=1:N_1, J=N_2:1, K=N_3:1 \\ I=N_1:1, J=1:N_2, K=1:N_3 \\ I=N_1:1, J=1:N_2, K=N_3:1 \\ I=N_1:1, J=N_2:1, K=1:N_3 \\ I=N_1:1, J=N_2:1, K=N_3:1 \end{array}, \tag{3}$$

where I, J and K are grid indices along the x_1, x_2 and x_3-axis, respectively, and N_i represents the number of grids in the model along the x_i-axis. In each of the eight sweepings, we obtain the solution to the Godunov upwind difference scheme-based equation using a recursive algorithm. The sweep iterations terminate once the difference between the solutions of two consecutive iterations are small enough.

For the adjoint-state variable, the adjoint-state traveltime equations based on the Lagrangian function are associated with

$$\nabla\left[\Lambda(\mathbf{x})\nabla T(\mathbf{x})\right]=0, \tag{4}$$

$$\Lambda(\mathbf{x}_r)n(\mathbf{x}_r)\cdot\nabla T(\mathbf{x}_r)=t(\mathbf{x}_r)-t_{obs}(\mathbf{x}_r), \tag{5}$$

where $\mathbf{x}_r$ represents the locations of receivers, and $\Lambda(\mathbf{x})$ represents the adjoint-state variable, and $T(\mathbf{x})$ is the traveltime computed under the current model $\mathbf{m}$ in equation (2). We solve this equation using equation (3) till convergence. Using the adjoint-state traveltime field $\Lambda(\mathbf{x})$, the gradient can be formulated as

$$\frac{\partial E(\mathbf{m})}{\partial v}=\sum_{N_s}\frac{\Lambda(\mathbf{x})}{v^3(\mathbf{x})}, \tag{6}$$

where N_s is the total number of sources.

2.2 3D Multiscale Elastic-Waveform Inversion

Elastic-waveform envelope inversion can produce a low-resolution initial velocity model for elastic-waveform inversion to improve the convergence. Analog to elastic-waveform inversion, envelope inversion fits data envelope $\mathbf{e}_{\text{obs}}$ with synthetic data envelope $\mathbf{e}_{\text{cal}}$ by minimizing the misfit function given by

$$E(\mathbf{m})=1-\frac{\int \mathbf{e}_{\text{obs}}(t)\mathbf{e}_{\text{cal}}(t)\,dt}{\sqrt{\int \mathbf{e}_{\text{obs}}^2(t)\,dt}\sqrt{\int \mathbf{e}_{\text{cal}}^2(t)\,dt}}, \tag{7}$$

where $\mathbf{m}$ is elastic parameters to be inverted, and t is time.

Elastic-waveform inversion progressively fits synthetic elastic waveforms $\mathbf{d}_{\text{cal}}$ with recorded elastic waveforms $\mathbf{d}_{\text{obs}}$ to obtain elastic parameters $\mathbf{m}$. The inversion minimizes the following zero-lag cross-correlation objective function:

$$E(\mathbf{m})=1-\frac{\int \mathbf{d}_{\text{obs}}(t)\mathbf{d}_{\text{cal}}(t)\,dt}{\sqrt{\int \mathbf{d}_{\text{obs}}^2(t)\,dt}\sqrt{\int \mathbf{d}_{\text{cal}}^2(t)\,dt}}. \tag{8}$$

The correlation-based misfit function can suppress some inversion artifacts caused by the difficulty in matching amplitudes of seismic waveforms in practical applications. Synthetic elastic-waveforms $\mathbf{d}_{\text{cal}}$ are related to model parameters $\mathbf{m}$ as

$$\mathbf{d}_{\text{cal}}=f(\mathbf{m}), \tag{9}$$

where f is the 3D elastic wavefield forward modeling operator. We use an optimized high-order staggered-grid finite-difference algorithm with convolutional perfectly matched layers for forward and backward propagation of wavefields in elastic-waveform inversion. In the data domain, low-frequency bandpass filtered data are used at earlier stages of inversion, producing a long-wavelength/low-resolution model. The inverted model is then used as the initial model at later stages of inversion of higher-frequency bandpass filtered

data to produce a shorter-wavelength/higher-resolution models. With gradually increased the frequency bands, all frequency contents of the observed data are eventually used for inversion. The objective function of this multiscale approach can be defined as:

$$E_m(\mathbf{m}) = 1 - \frac{\int W(\omega)\mathbf{d}_{\text{obs}}(\text{t}) W(\omega)\mathbf{d}_{\text{cal}}(\text{t})\,\text{dt}}{\sqrt{\int \left[W(\omega)\mathbf{d}_{\text{obs}}(\text{t})\right]^2 \text{dt}}\sqrt{\int \left[W(\omega)\mathbf{d}_{\text{cal}}(\text{t})\right]^2 \text{dt}}} \tag{10}$$

with the frequency-dependent weights defined as

$$W(\omega) = \begin{cases} 1, & \text{if } \omega_{\min} \le \omega \le \omega_{\max} \\ 0, & \text{if } \omega > \omega_{\min} \text{ or } \omega < \omega_{\max} \end{cases}, \tag{11}$$

where $\omega_{\min}$ and $\omega_{\max}$ are the minimum and maximum frequencies of a frequency band, respectively. In the time-domain elastic-waveform inversion, this scheme is implemented by filtering observed and synthetic data before the gradient computation using the adjoint-state method.

2.2 3D Elastic Least-Squares Reverse-Time Migration

We use an elastic least-squares reverse-time migration method with implicit wavefield separation (Gao et al., 2017) to produce subsurface images using the VSP field data. Our ELSRTM method is based on elastic-waveform inversion (EWI) and efficient Hilbert-transform-based implicit wavefield separation. We use our new method to invert for the high-wavenumber model perturbations. Elastic model $\mathbf{m}$ is composed of two components:

$$\mathbf{m} = \mathbf{m}_0 + \Delta\mathbf{m}, \tag{12}$$

where $\mathbf{m}_0$ is the low-wavenumber background parameter model, and $\Delta\mathbf{m}$ is the high-wavenumber model perturbation. Seismic reflection wavefields are elastic waves scattered/reflected by $\Delta\mathbf{m}$. We obtain the model parameter gradients of the misfit function $E(\mathbf{m})$ for ELSRTM as

$$\frac{\partial E(\mathbf{m})}{\partial \Delta V_p} = \sum_{N_s, N_r} (-2\rho V_p) \int_0^T \begin{bmatrix} W\left(\partial_t \varepsilon_{xx}, \varepsilon_{xx}^{\dagger}\right) + W\left(\partial_t \varepsilon_{yy}, \varepsilon_{yy}^{\dagger}\right) + W\left(\partial_t \varepsilon_{zz}, \varepsilon_{zz}^{\dagger}\right) \\ + W\left(\partial_t \varepsilon_{xx}, \varepsilon_{zz}^{\dagger}\right) + W\left(\partial_t \varepsilon_{zz}, \varepsilon_{xx}^{\dagger}\right) + W\left(\partial_t \varepsilon_{yy}, \varepsilon_{zz}^{\dagger}\right) \\ + W\left(\partial_t \varepsilon_{zz}, \varepsilon_{yy}^{\dagger}\right) + W\left(\partial_t \varepsilon_{xx}, \varepsilon_{yy}^{\dagger}\right) + W\left(\partial_t \varepsilon_{yy}, \varepsilon_{xx}^{\dagger}\right) \end{bmatrix} dt, \tag{13}$$

$$\frac{\partial E(\mathbf{m})}{\partial \Delta V_s} = \sum_{N_s, N_r} (-2\rho V_s) \int_0^T \begin{bmatrix} W\left(\partial_t \varepsilon_{xz}, \varepsilon_{xz}^{\dagger}\right) - 2W\left(\partial_t \varepsilon_{xx}, \varepsilon_{zz}^{\dagger}\right) - 2W\left(\partial_t \varepsilon_{zz}, \varepsilon_{xx}^{\dagger}\right) \\ + W\left(\partial_t \varepsilon_{yz}, \varepsilon_{yz}^{\dagger}\right) - 2W\left(\partial_t \varepsilon_{yy}, \varepsilon_{zz}^{\dagger}\right) - 2W\left(\partial_t \varepsilon_{zz}, \varepsilon_{yy}^{\dagger}\right) \\ + W\left(\partial_t \varepsilon_{xy}, \varepsilon_{xy}^{\dagger}\right) - 2W\left(\partial_t \varepsilon_{xx}, \varepsilon_{yy}^{\dagger}\right) - 2W\left(\partial_t \varepsilon_{yy}, \varepsilon_{xx}^{\dagger}\right) \end{bmatrix} dt, \tag{14}$$

where V_p and V_s are P- and S-wave velocities, respectively, $\varepsilon_{ij} = s_{ijkl}\sigma_{kl}$ is the strain wavefield, and † represents the adjoint-state wavefield. The elastic compliance s_{ijkl} can be expressed with elasticity parameters C_{IJ} under the Voigt notation and further expressed with V_p, V_s and the density ρ. The wavefield-separation operation W on the right hand side of equation (13) and (14) reads:

$$W(u,v) = uv - H_z(u)H_z(v), \tag{15}$$

where H_z is the Hilbert transform along the depth.

3. RESULTS

3.1 Walkaway VSP Data

In 2016, we conducted a VSP survey at the Raft River geothermal field along five walkaway lines using 84 three-component (3C) receivers and 145 vibroseis sources, approximately 30 sources along each walkaway line. The receivers were deployed in well RRG-9 from depths of 400 m to 1500 m. The 145 vibroseis sources were located at five walkaway lines (Figure 3) along different azimuths from well RRG 9. The receiver interval is approximately 15 m, and the source interval ranges from 30 to 60 m.

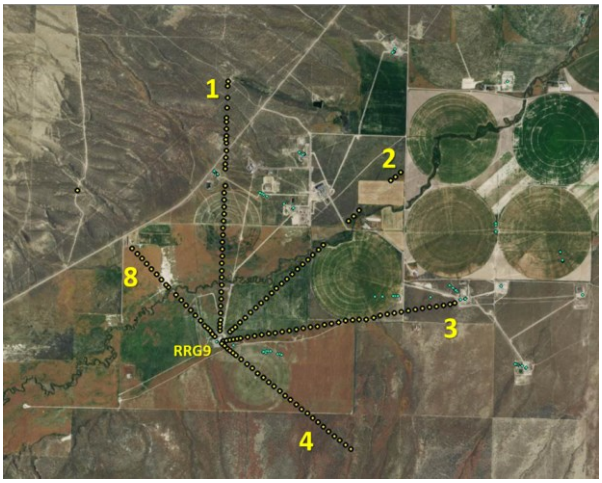

Figure 3: Five walkaway VSP lines around well RRG-9 at the Raft River geothermal field.

To perform our elastic-waveform inversion and elastic least-squares reverse-time migration, we first rotate and denoise the correlated VSP data. Figure 4-5 show the correlated, rotated and denoised three-component VSP data for a shot with offset of 1000m on Line 4.

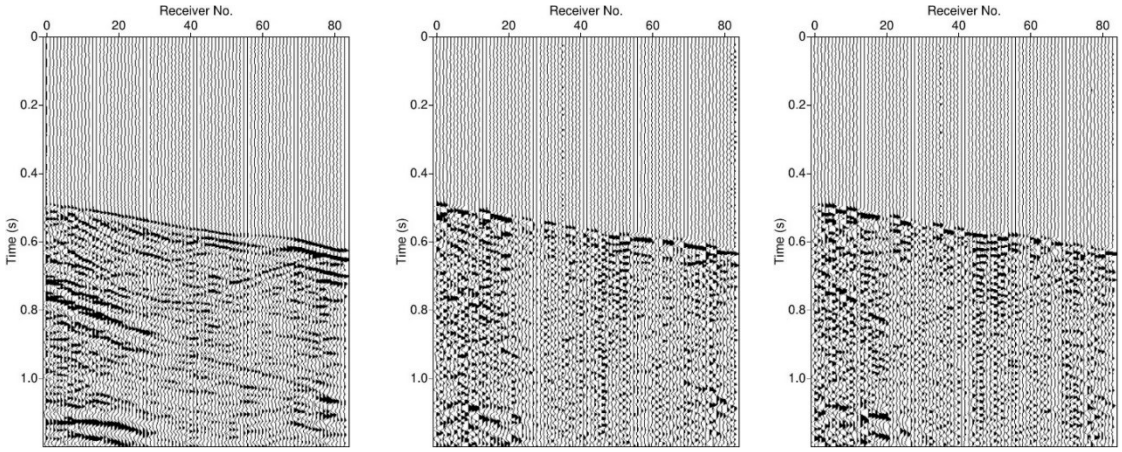

Figure 4: Three-component VSP data for a shot with an offset of 1000m on Line 4: vertical component (left panel), horizontal-one (Hx) component (middle panel), and horizontal-two (Hy) component (right panel).

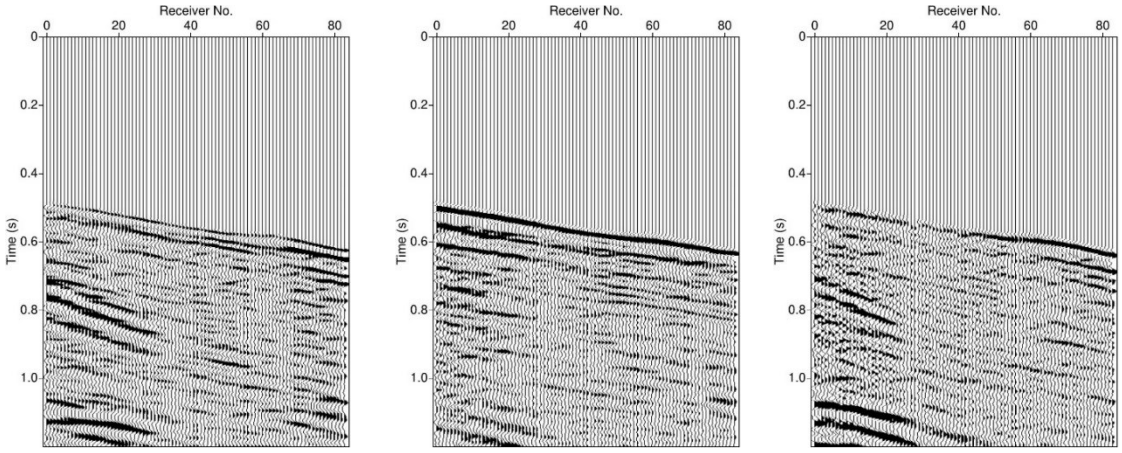

Figure 5: Rotated and denoised three components of VSP data for a shot with an offset of 1000m on Line 4: vertical component (Vz wavefield) (left panel), aligned horizontal component (Hx wavefield) (middle panel), and perpendicular horizontal component (Hy wavefield) (right panel).

3.2 3D First-Arrival Traveltime Tomography of Downgoing VSP Waves

We build a 1D velocity model using sonic log data from RRG-9 collected in 2012 and 1D traveltime tomography inversion of first arrivals of zero-offset VSP data. The resulting 1D velocity model is shown in Figure 6.

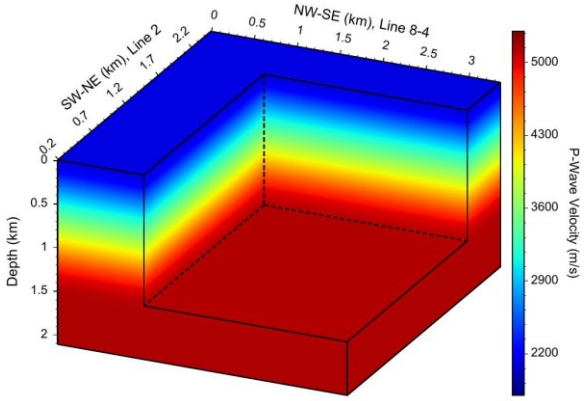

Figure 6: Initial 1D P-wave velocity model obtained from sonic log data and 1D traveltime tomography of zero-offset VSP data.

To account for lateral variations in the velocity model, we conduct 3D traveltime tomography using the 1D velocity model (Figure 6) as the initial model. We use the first-arrival traveltime of the down-going p-waves of the VSP data from five walkaway lines to conduct 3D traveltime tomography. After 30 iterations, the root-mean-square (RMS) residual of traveltime decreases to 2% of the initial value calculated from the 1D initial model. The velocity model in Figure 7 shows a low-velocity zone near the center of the model. This low-velocity zone may be associated with the Narrows zone.

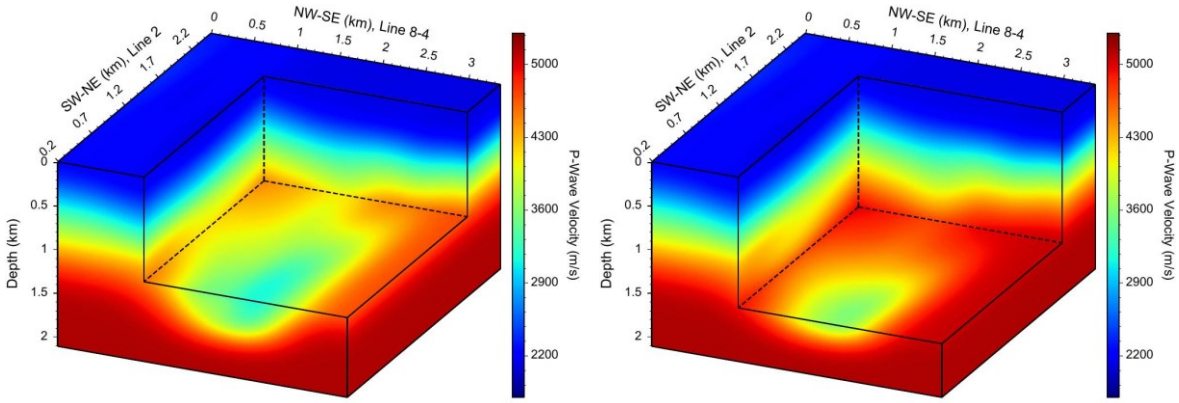

(a) Horizontal cut at depth of 1.2 km (b) Horizontal cut at depth of 1.5 km

Figure 7: 3D velocity model obtained using traveltime tomography of first arrivals of VSP down-going waves along five walkaway lines

3.3 Multiscale Elastic-Waveform Inversion

We apply our multiscale elastic-waveform inversion method (Chi and Huang, 2018a) to the rotated and denoised 3C VSP field data collected along five walkaway lines to further improve the velocity models. Our elastic-waveform inversion uses the 3D traveltime tomography velocity model as the initial model. We invert VSP data in the frequency bands with an upper frequency of 10, 15, 20 and 25 Hz, and show our final elastic-waveform inversion results of 3D compressional- (P-) and shear-wave (S-wave) velocity models in Figure 8 and 9 at two different depths. Our elastic-waveform inversion results further refine the elastic velocity models showing the low-velocity zone near the center of the model.

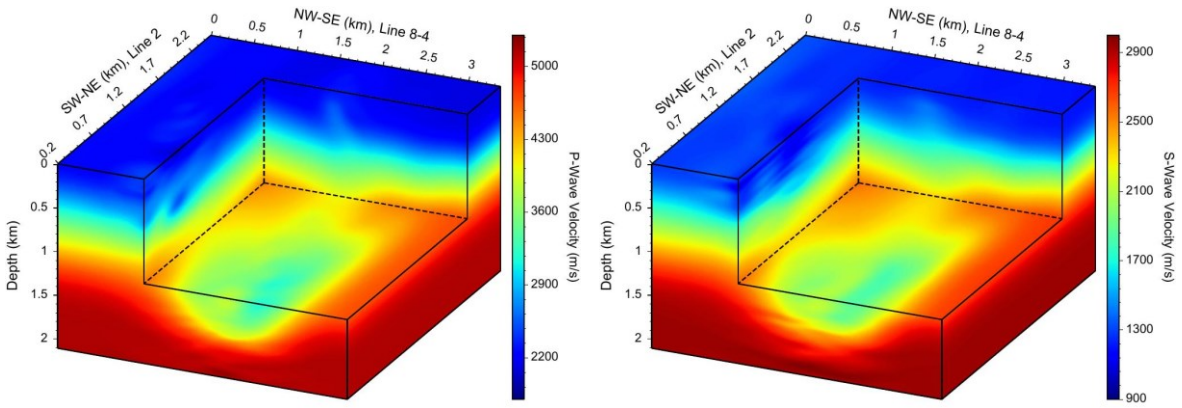

(a) Inverted 3D P-wave velocity model (b) Inverted 3D S-wave velocity model

Figure 8: 3D multiscale elastic-waveform inversion results of Vp (a) and Vs (b) models, where the horizontal cut is at 1.2 km in depth.

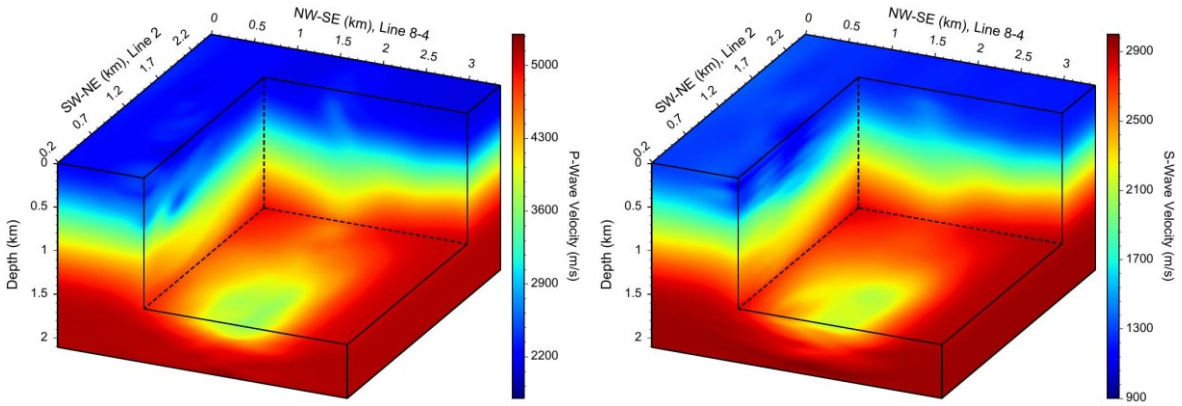

(a) Inverted 3D P-wave velocity model (b) Inverted 3D S-wave velocity model

Figure 9: 3D multiscale elastic-waveform inversion results of Vp (a) and Vs (b) models, where the horizontal cut is at 1.5 km in depth.

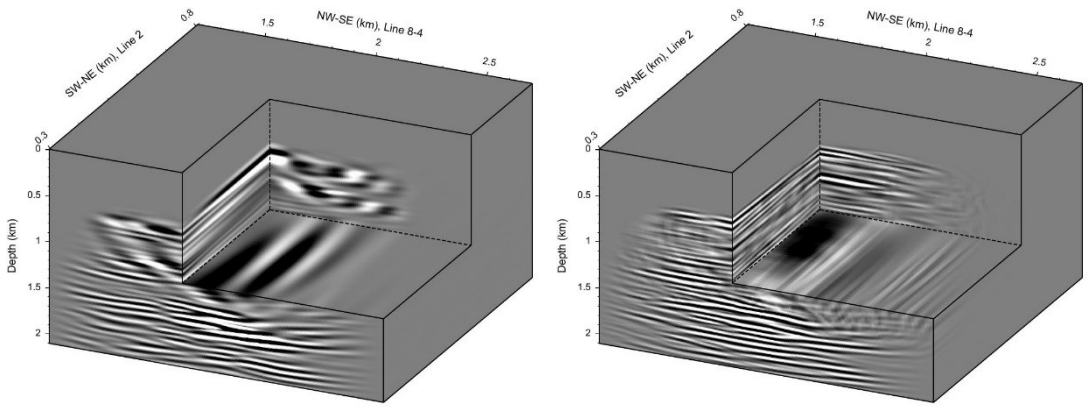

(a) 3D P-wave image (b) 3D S-wave image

Figure 10: P- (a) and S- (b) images obtained using 3D least-squares elastic reverse-time migration of the VSP data, where the horizontal cut is at 1.2 km in depth.

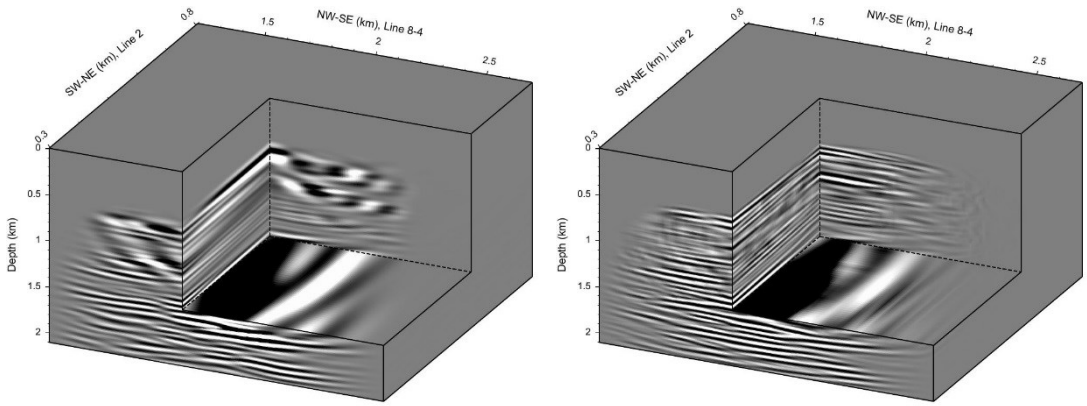

(a) 3D P-wave image (b) 3D S-wave image

Figure 11: P- (a) and S- (b) images obtained using 3D least-squares elastic reverse-time migration of the VSP data, where the horizontal cut is at 1.5 km in depth.

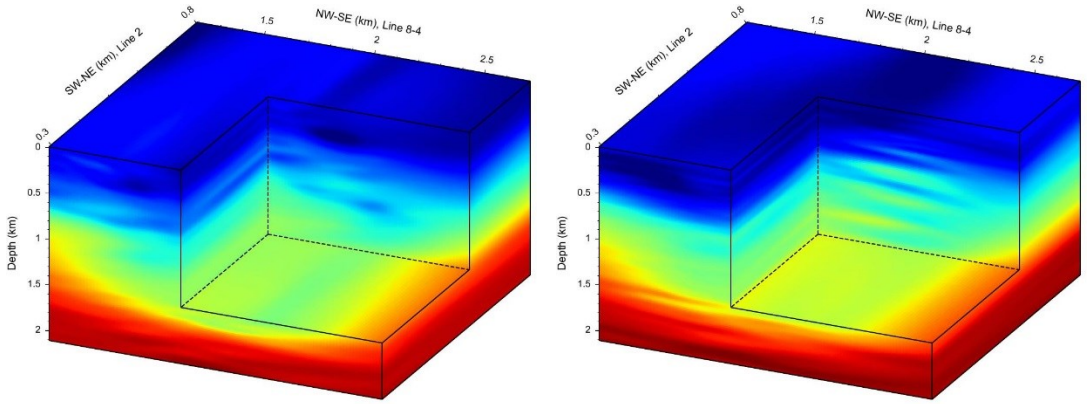

(a) Inverted 3D P-wave velocity model (b) Inverted 3D S-wave velocity model

Figure 12: Zoomed in 3D multiscale elastic-waveform inversion results of Vp (a) and Vs (b) models, with the same display area as the ELSRTM results in Figure 11.

3.3 3D Elastic Least-Squares Reverse-Time Migration

We apply ELSRTM to the 3C VSP data to obtain 3D migration images using the multiscale elastic-waveform inversion inverted P- and S-wave velocity models. We show the 3D migration images in Figure 10 and 11. Some fault zones can be recognized from the high-resolution images, consist with the low velocity zone inverted using elastic waveform inversion (Figure 12), which may be associated with the Narrows zone, which is the geothermal stimulation zone.

4. CONCLUSIONS

We haves successfully obtained the high-resolution velocity models and migration images of the subsurface structures at the Raft River geothermal field using the 2016 walkway 3C VSP data. We have first built an initial velocity model using sonic logging data, zero-offset VSP data and first-arrival times of down-going waves in the walkaway VSP data. We have then used this initial model to conduct 3D multiscale elastic-waveform inversion of the VSP data to improve P- and S-wave velocity models. Our inversion results show a low-velocity zone in both the compressional- and shear-wave velocity models. This low-velocity zone may be associated with the Narrows zone that is the geothermal stimulation zone. In addition, we have applied 3D elastic least-squares reverse-time migration to the VSP field data and obtained high-resolution P- and S-wave migration images. Some fault zones can be recognized from the high resolution images, which are consistent with the low velocity zone inverted using elastic-waveform inversion.

5. ACKNOWLEDGMENTS

This work was supported by the Geothermal Technologies Office (GTO) of the U.S. Department of Energy through contract DE-AC52-06NA25396 to Los Alamos National Laboratory (LANL). This research used resources provided by the Los Alamos National Laboratory Institutional Computing Program, which is supported by the U.S. Department of Energy National Nuclear Security Administration under Contract No. 89233218CNA000001.

REFERENCES

Ayling B., P. Molling, R. Nye and J. Moore, 2011, Fluid geochemistry at the Raft River geothermal field, Idaho: new data and hydrogeological implications: Proceedings, 36th Workshop on Geothermal Reservoir Engineering, SGP-TR-191.

Ayling, B., and Moore, J.: Fluid geochemistry at the Raft River geothermal field, Idaho, USA: New data and hydrogeological implications, *Geothermics*, **47**, (2013), 116-126.

Chi, B., and Huang, L. "Multiscale elastic-waveform inversion of 2016 walkway VSP data from the Raft River geothermal field." *Proceedings: 43rd Workshop on Geothermal Reservoir Engineering*, Stanford University, Stanford, CA (2018a), SGP-TR-213.

Chi, B., and Huang, L. "Least-squares reverse-time migration of walkaway VSP data from the Raft River geothermal field." *GRC Trans*actions, **42**, (2018b).

Gao, K., Chi, B. and Huang, L. "Elastic least-squares reverse-time migration with implicit wavefield separation." *Proceedings, SEG Technical Program Expanded Abstracts*, (2017).

Jones C., J. Moore, W. Teplow and S. Craig, 2011, Geology and hydrothermal alteration of the Raft River geothermal system, Idaho: Proceedings, 36th Workshop on Geothermal Reservoir Engineering, SGP-TR-191.

Li, D., Huang, L., Jones, C., Moore, J., Freeman, K., Majer, E.: 3D Inversion of MT Data from the Raft River Geothermal Field: Preliminary Results, *GRC Trans*actions, **36**, (2017).

Mabey, D. R., D. B. Hoover, J. E. O'Donnell, and C. W. Wilson, 1978, Reconnaissance geophysical studies of the geothermal systems in southern Raft River valley, Idaho: Geophysics, 43, 1470-1484.

Williams, P., Covington H. R., and Pierce, K. L. "Cenozoic stratigraphy and tectonic evolution of the Raft River basin, Idaho, in Cenozoic Geology of Idaho." *Idaho Bureau of Mines and Geology Bulletin*, 26, (1982), 491-504